PHYSICAL REVIEW A **75**, 042711 (2007)

Water-molecule dissociation by proton and hydrogen impact

H. Luna,[1,*] A. L. F. de Barros,[2] J. A. Wyer,[3] S. W. J. Scully,[3] J. Lecointre,[4] P. M. Y. Garcia,[5] G. M. Sigaud,[5] A. C. F. Santos,[6] V. Senthil,[3] M. B. Shah,[3] C. J. Latimer,[3] and E. C. Montenegro[6]

[1]*NCPST and School of Physical Science, Dublin City University, Glasnevin, Dublin 9, Republic of Ireland*
[2]*Departamento de Ensino Superior, Centro Federal de Educação Integrada Celso Suckow da Fonseca, Av. Maracanã 229, Rio de Janeiro, RJ 20271-110, Brazil*
[3]*Department of Pure and Applied Physics, Queen's University of Belfast, Belfast, Northern Ireland, United Kingdom*
[4]*Département de Physique, unité PAMO, Université Catholique de Louvain, Chemin du Cyclotron 2, B-1348 Louvain-la-Neuve, Belgium*
[5]*Departamento de Física, Pontifícia Universidade Católica do Rio de Janeiro, Cx. Postal 38071, Rio de Janeiro, RJ 22452-970, Brazil*
[6]*Instituto de Física, Universidade Federal do Rio de Janeiro, Caixa Postal 68528 Rio de Janeiro, 21945-970, RJ, Brazil*

(Received 26 January 2007; published 18 April 2007; corrected 25 April 2007)

Time-of-flight-based mass analysis of charged water fragments have been used to measure the dissociative and the nondissociative reaction pathways of water formed during collisions with 15 to 100 keV and 500 to 3500 keV H^+ projectiles and with 8 to 100 keV H^0 projectiles. The fragmentation pathways resulting from the ionization and the electron capture collisions with the incident H^+ and H^0 projectiles, as well as collisions involving projectile electron loss by the incident H^0 projectiles, were separately recorded by detecting the target product ions in coincidence with either the ejected target electrons or the charge-analyzed projectiles. The fragmentation profile shows that at high collision energies the ionization of water arises mainly through outer shell processes. At lower energies valence electron capture and ionization dominate and transfer ionization leads to substantially different fragmentation patterns. H^0 and H^+ projectiles are found to be equally efficient at ionizing the water molecule. These results are of particular interest to workers in astrophysics and those involved in cancer therapy with heavy particle ion beams.

DOI: 10.1103/PhysRevA.75.042711 PACS number(s): 34.50.Fa, 52.20.Hv

I. INTRODUCTION

Collision-induced fragmentation of water by energetic hydrogen projectiles has received considerable attention in recent years mainly due to the very important role that water ions and its ionic and neutral radicals play in proton-based cancer therapies as facilities such as these become more widely available. In addition, the recent data sent by the various space probes to Saturn and Mars also require more detailed information on water dissociation in the quest to find answers concerning the presence of water on these planets and the implications on other regions of the Universe. For instance, the oxygen-rich atmosphere of Europa is supposed to be a result from collision-induced dissociation of water [1]. Furthermore, fundamental interest on this collision system continues to remain strong in a bid to properly test the wave functions and the potential energy curves of the water molecule in isolated form and in the liquid phase [2].

The radiolysis of water and the damage that the highly reactive radical products, such as H, O, and OH fragments, both in their neutral and ionized forms cause to living cells has been the main impetus behind the present measurements [3]. As much as 70% of the damage produced during irradiation is thought to come from interactions of such species produced during the numerous collisions that the incident radiation make with the abundant water in the cell [4]. The radicals are thought to combine and produce the inflammatory oxidant H_2O_2, which acts as an inhibitor or a promoter of apoptosis [5]. Also in calculations such as the event-by-event Monte Carlo track structure simulations [6,7], the data are used to assess the slowing down of the proton tracks and the amount of linear energy transfer (LET) that the projectiles deposit in the cell. Of particular interest are the data over the energy range 1 keV to 1 MeV corresponding to the energies which the hydrogen projectiles tend to have around the Bragg peak. However, water radiolysis data is currently not available for incident protons over this energy range and, consequently, such models are unable to assess the precise extent of the damage caused around the Bragg peak. Furthermore, below the 50-keV region of the Bragg peak, the hydrogen projectile beam starts to contain a substantial amount of atomic H^0 components and thus data for the fast neutral hydrogen species are also required for accurate modeling. To the best of the authors' knowledge, no radiolysis measurements are available for these H^0 species.

In the present paper we denote the cross sections for the following collision process:

$$H^{k+} + H_2O \rightarrow H^{m+} + [H_2O]^{n+} + (m+n-k)e$$

by σ_{km}, where $k=0$ or 1 with the final fast beam projectile charge m being measured only and by ${}_{k0}\sigma_{mn}$ when both the projectile final charge m and the water target product ions $[H_2O]^{n+}$, which includes the fragment ions H^+, OH^+, and O^+, as well as H_2O^+, are measured through coincidence methods.

Toburen *et al.* [8] reported the first cross sections for total one-electron capture (σ_{10}) and total one-electron loss (σ_{01}) for incident protons and neutral hydrogen atoms, respectively, on the water molecule. Rudd *et al.* [9] extended this

---

[*] Corresponding author.

data, measuring total cross sections for target positive ion production (σ_+), target electron production (σ_-), and one-electron capture (σ_{10}) for incident protons over the energy range 7 to 5000 keV. Later, Werner *et al.* [10] employed a time-of-flight coincidence and imaging detection techniques to measure individual water dissociation products during ionizing collisions with fast protons over the 100 to 350 keV incident energy range. More recently, Gobet *et al.* [11] carried out dissociative and nondissociative cross section measurements at lower energies (20 to 150 keV) by proton impact using a time-of-flight coincidence technique to separately record the cross sections arising from ionizing and electron capture collisions. As will be discussed later, Gobet *et al.* [11,12] used large species-dependent correction factors to obtain their cross sections for channels leading to H^+, O^{2+}, O^+, and OH^+ target ion formation.

The Bragg peak maximum for protons is found to be around 100 keV with the portion of the peak beyond 100 keV dominated entirely by ionization collision processes and that below 100 keV dominated both by the electron capture and the ionization processes. Below 30 keV the peak is dominated almost entirely by the electron capture processes. Scaling laws are relatively easier to devise for ionization processes with the result that proton therapy dose profiles are being accurately predicted over the high-energy regions of the Bragg peak. However, scaling laws are often difficult to obtain for capture processes, especially when dissociation is involved, and experimental measurements are the only available resort to obtain this kind of data for accurate modeling of the dose profiles below the Bragg peak maximum. In this work we have used an improved time-of-flight coincidence counting arrangement to perform dissociative and nondissociative measurements of water by proton and neutral hydrogen impact over the 8 to 100 keV energy range and by proton impact over the 500 to 3500 keV energy range. The high-energy measurements were carried out for the direct ionization channel $H^+ \rightarrow H^+$ only, while the low-energy proton measurements were carried out for the one-electron capture channel $H^+ \rightarrow H^0$ and for the ionization channel involving the ejection of at least one target electron. The latter measurements, consequently, include contributions from the pure ionization channel $H^+ \rightarrow H^+$ and the transfer-ionization channel $H^+ \rightarrow H^0 + e$. For neutral hydrogen impact, the measurements were carried out for the direct ionization channel $H^0 \rightarrow H^0$, the electron-loss channel $H^0 \rightarrow H^+$, and the single electron capture channel $H^0 \rightarrow H^-$.

II. EXPERIMENT

A. High-energy measurement setup

The experimental setup used for the high-energy measurement has been described previously [13,14] and only the most important features will be given here. Proton beams with energies ranging from 500 to 3500 keV extracted from the Catholic University of Rio de Janeiro 4 MV Van de Graaf accelerator were directed by a 90° magnet followed by a switching magnet onto a narrow collimator 1.5 m upstream of the experimental chamber and offset from the beam line axis. A third magnet placed after the collimator was used to bend the proton beam through a second narrow on-axis collimator placed close to the interaction region to remove neutral components formed in the beam from collisions with upstream background gas. After traversing the interaction region, a fourth magnet directed the proton beam onto a position-sensitive microchannel plate (MCP) detector placed 4 m downstream. A thick Al diffuser in front of the detector ensured the entire sensitive area of the detector was illuminated uniformly thereby permitting the detector to operate at high counting rates [order of $(15-30) \times 10^3$ particles/sec].

In these high-energy measurements, the target gas was contained within a cell. A pair of parallel plates housed within the cell extracted the target products through a grid placed over a hole in one of the plates. The extracted ions traveled through a drift region and onto a second MCP detector assembly. A strong extraction field of 960 V/cm was used to ensure complete collection of all the target products. Coincidences between the fast detector and the slow target ion detector provided the dissociative and the nondissociate measurements resulting for pure ionization collisions. No attempt was made to make measurements for the electron capture channel as the fast neutral signal in this energy range was found to be negligibly small. See Cavalcanti *et al.* [15] for more details.

B. Low-energy measurement setup

These measurements were carried out using the Queen's University Belfast 100 keV accelerator facility. A crossed-beam arrangement involving the intersection of the projectile beam with the target beam at 90° was used. A pair of open geometry conical electrodes containing high transparency grids surrounded the intersection region and extracted the target products. The extracted ions were focused by a lens system and were detected by an MCP detector assembly, while the electrons extracted in the opposite direction were detected by a channeltron detector. The projectile products were separated from the main proton beam by a set of deflection plates placed downstream of the interaction region and were detected by a second channeltron. The proton beam was detected in a shielded Faraday cup. See Luna *et al.* [16,17] for more experimental details. In measurements involving one-electron capture with a proton beam, we found it extremely important to use a set of three small deflection plates to wiggle the proton beam just prior to the interaction region and clean it of neutrals formed upstream in collisions with the background gas. For the collisions involving H^0 projectiles, a neutral beam was formed by partially neutralizing the proton beam inside an upstream gas cell and deflecting away any remaining protons by a deflection-plate assembly placed at the position of the wiggler plates. A substantial fraction of the neutral atoms formed in the upstream gas cell is not in the ground state. Taking into consideration the distance from the cell to the target chamber and the projectile velocities used, we have found that the time-of-flight was long compared to radiative lifetime of all H_0 atoms with $n \leqslant 6$ except those in the metastable $2s$ state. The $2s$ component of the neutral beam was eliminated by the same deflection plates used to clean the charged part of the beam. The

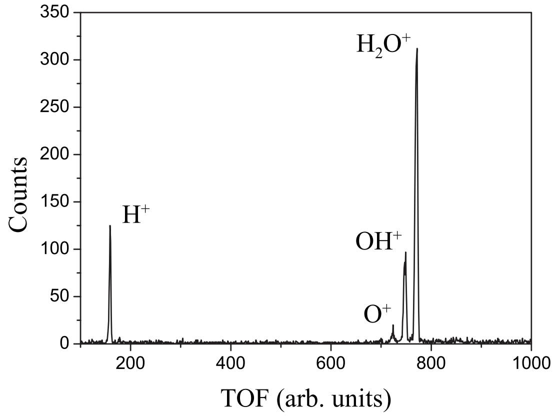

FIG. 1. TOF spectrum for 2 MeV protons incident on water vapor taken with the experimental setup at the Catholic University of Rio de Janeiro.

applied 5 kV/cm electric field is strong enough to quench the H(2*s*) component to the ground state [18,19]. The Faraday cup was replaced by a secondary emission detector, comprising of a negatively biased angled plate to repel secondary electrons generated by the incident projectiles and a surrounding plate that collected the repelled electrons. The detector was calibrated assuming the response was the same for both fast ions and fast atoms [20]. For both the incident proton and neutral beams, measurements of the target products were carried out in coincidence with either the fast projectile products or the ejected target electrons. Extraction fields of 250 V/cm were found to be necessary to collect all the target product ions without appreciably deflecting the incident proton beam or the protons formed from the neutral beam in the interaction region in electron loss collisions. The deflection problems were particularly severe at low collision energies.

The target gas was fed from a completely out-gassed reservoir of water in controlled amounts via a needle valve into a static target gas cell in our high-energy measurements and into a bunch of 1 mm-diameter tubes to form a 5 mm collimated beam in the interaction region, in our low-energy measurements. The tubes housed in a separate differentially pumped chamber were 10 mm in length and were set within a 4 mm-diameter tube. The time-of-flight (TOF) coincidence spectra were recorded using a time-to-amplitude (TAC) unit operated with start pulses from either the fast projectile detector or the target electron detector and the stop pulses from the slow target ion detector. Figure 1 shows our measured TOF spectrum for 2 MeV protons. This setup allowed us to work in a single-hit configuration. Further discussions about detection efficiencies and contribution from double ion formation will be given in Sec. III.

C. Normalization

Cross sections ${}_{10}\sigma_{0n}$ for each of the target channels involving one electron capture can be given by the expression

$$ {}_{10}\sigma = \sum_{n} {}_{10}\sigma_{0n} = \frac{S_c}{k^+ k_p \mu}, \tag{1}$$

where S_c is the areas under the H^+, O^+, OH^+, and H_2O^+ ion peaks such as in Fig. 1, or a combination of them when more than one electron is removed leading to double ion fragment formation, per unit current and unit pressure, recorded with start pulses supplied to TAC from the fast projectile detector and the stop pulses supplied from the target ion detector. k^+ and k_p are the detection efficiencies of the target ions and of the fast projectiles detectors, respectively, and $\mu = nl$, where n is the target number density and l the target thickness traversed by the proton beam. The product $k^+ k_p \mu$ was obtained by normalizing our summed signal for all the channels to the total one-electron capture cross sections σ_{10} of Rudd *et al.* [9], which have an estimated uncertainty of 8%. Our high-energy ionization cross sections ${}_{10}\sigma_{1n}$ for each channel were also obtained from this equation with ${}_{10}\sigma_{0n}$ replaced with ${}_{10}\sigma_{1n}$ and S_c by the signal S_i obtained from spectra recoded with protons falling directly on the fast projectile detector. The factor $k^+ k_p \mu$ in these measurements was determined by normalizing our summed signal to Rudd *et al.* [9] σ_+ (total) cross sections. At these energies (>500 keV) capture processes are negligible, so that σ_+ should correspond almost entirely to ${}_{10}\sigma_{1n}$.

For our spectra recorded with start pulses from the target electron detector and the stop from the target ion detector, the cross sections σ_e for collision channels involving target electron production is given by

$$\sigma_e = \frac{S_e}{k^+ k^- \mu}, \tag{2}$$

where S_e is the area under the individual H^+, O^+, OH^+, and H_2O^+ ion peaks or as Eq. (1), a combination of the peaks, in the recorded spectra, and k^- is the detector efficiency of the target electron detector. The factor $k^+ k^- \mu$ was determined in the following way by considering only the H_2O^+ peak in the following way: At the collision energy of 100 keV, the continuously operated proton beam was replaced by a pulsed beam of protons 150 nsec in width and 10^5 Hz repetition rate and the spectra were recorded with the start pulses supplied from the pulsed-beam generator. The stop pulses were supplied from the target ion detector as before. The area $S_+(H_2O^+)$ under the H_2O^+ peak obtained with the pulsed beam measurements then corresponded to the production of total positive H_2O^+ ions and to the cross sections $\sigma_+(H_2O^+)$ given by the expression

$$\sigma_+(H_2O^+) = \frac{S_+(H_2O^+)}{k^+ \mu}. \tag{3}$$

The extraction field was kept constant and of similar value to that of the contentiously operated beam mode. In the pulsed-beam mode the O^+, OH^+, and H_2O^+ ion peaks were found to merge into one another and remained unresolved. However, since the H_2O^+ peak was the largest, the contribution to this peak was assessed with a reasonable degree of confidence using our ratios obtained in measurements without pulsing. If we take the detection efficiency of our fast projectile channeltron detector k_p to be almost unity at 100 keV then Eq. (1) essentially becomes

TABLE I. Cross sections (in Mb) for proton impact ionization of H_2O over the 15 to 100 keV and the 500 to 3500 keV energy ranges. The 500 to 3500 keV energy range cross sections are for pure ionization. The 15 to 100 keV energy range cross sections also include contributions from the transfer-ionization process.

E (keV)	H_2O^+	OH^+	H^+	O^+
15	153±15	62±9	131±20	14.8±3
22.5	219±23	86±13	175±26	24±4
30	235±28	100±15	187±28	26±4
40	240±28	97±14	179±27	22±4
50	262±31	111±16	179±27	25±4
60	273±30	101±15	165±24	25±4
70	279±33	84±12	155±23	24±3
80	279±33	90±12	147±22	22±3
100	273±33	78±12	125±19	20±3
500	97±14	43±6	33.1±4.8	5.6±1.2
750	76±11	22±3	20.6±2.9	3.3±0.8
1000	68±10	21±3	16.2±2.4	2.7±0.5
1500	51±6	16±2	14.0±1.6	2.4±0.3
2000	45±6	13±2	10.5±1.5	1.8±0.4
2500	35±5	9.3±1.3	7.8±1.5	1.2±0.2
3000	31±4	7.9±1.1	8.4±1.6	
3500	27±3	6.6±1.0	6.5±0.9	

$$_{10}\sigma_{01} = S_c/k^+\mu. \tag{4}$$

$\sigma_+(H_2O^+)$ can then be calculated from the ratio of $S_+(H_2O^+)$ and summed S_c in Eqs. (3) and (4) and Rudd *et al.* value σ_c (total) at 100 keV. Since H_2O^+ can only arise from a pure capture collision or a pure ionization collision (i.e., the H_2O^+ signal contains no transfer ionization contributions), the pure ionization cross section $_{10}\sigma_{11}(H_2O^+)$ for H_2O^+ is given by

$$_{10}\sigma_{11}(H_2O^+) = \sigma_+(H_2O^+) - \sigma_{10}(H_2O^+), \tag{5}$$

where the $\sigma_+(H_2O^+)$ and the $\sigma_{10}(H_2O^+)$ can be obtained from the total cross sections of Rudd *et al.* [9] using the ratios of our measured partial cross sections. Thus, by replacing σ_e in Eq. (2) with $_{10}\sigma_{11}(H_2O^+)$ from Eq. (5) and S_+ with $S_+(H_2O^+)$, the product $k^+k^-\mu$ is obtained.

III. RESULTS AND DISCUSSION

A. Proton impact

Our results for dissociative (radiolysis of water) and non-dissociative (involving parent molecule remaining intact) channels resulting from one-electron capture and ionization collisions of water molecule by protons are given in Table I and Table II, respectively, and are shown in Figs. 2 and 3, respectively. The error bars for our high-energy measurements are mainly due to counting statistics and the reproducibility of our measurements, while, for our low-energy measurements, the uncertainties are mainly due to the difficulty of obtaining mass spectra with fully resolved O^+, OH^+, and H_2O^+ peaks. In this case, we were restricted to use small extraction voltages in order to keep the deflection experienced by the projectile beam within acceptable values. The H^+ peak was fully resolved and the uncertainties for this channel, on the other hand, come mainly from our inability to ascertain whether all the trajectories of ions carrying large amounts of the dissociation energy fell within the detector surface area. Being the lightest, these ions receive most of the dissociation energy, which can be in excess of 10 eV (c.f., Alvarado *et al.* [21]). As will be discussed later, we carried out several tests to ensure that collection of the H^+ ions was maximized.

TABLE II. Cross sections (in Mb) for one electron capture by 15 to 100 keV protons in H_2O.

E (keV)	H_2O^+	OH^+	H^+	O^+
15	437±54	122±22	111±17	18±3
22.5	421±52	139±25	150±23	22±3
30	315±39	118±21	151±23	26±4
40	217±27	88±16	136±21	22±4
50	167±21	72±13	124±19	22±3
60	126±16	54±9	104±16	18±3
70	92±11	43±8	81±12	14±2
80	73±12	36±8	63±10	14±2
100	45±6	21±4	40±6	7±1

The cross sections for the combined pure one-electron capture $_{10}\sigma_{01}$ and transfer ionization $_{10}\sigma_{02}$ leading to H_2O^+, OH^+, O^+, and H^+ target products are shown in Fig. 2.

As can be seen, at our lowest energy, one-electron capture collisions are dominated entirely by the channel leading to H_2O^+ formation, followed by the channels leading to OH^+ and H^+, each about a factor of 4 smaller, and the channel leading to O^+, smaller by approximately two orders of magnitude. Around 100 keV, however, the cross sections for the

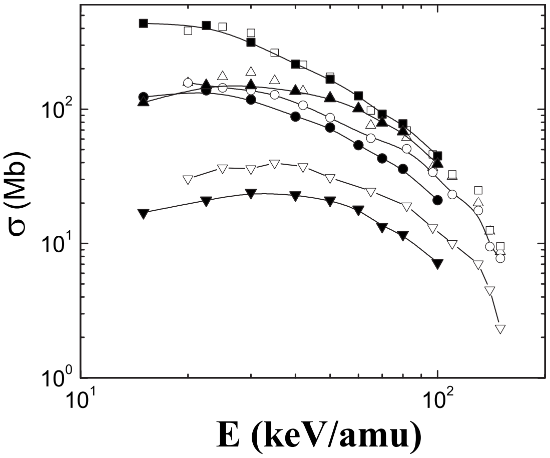

FIG. 2. H^+ impact capture cross sections for combined $_{10}\sigma_{01} + {}_{10}\sigma_{02}$ leading to the formation of the target products H_2O^+, OH^+, O^+, and H^+. Present data—filled symbols; Gobet *et al.* [11,12]—open symbols. Key: squares—H_2O^+; up triangles—H^+; circles—OH^+; inverted triangles—O^+. Error bars are not shown for the sake of clarity.

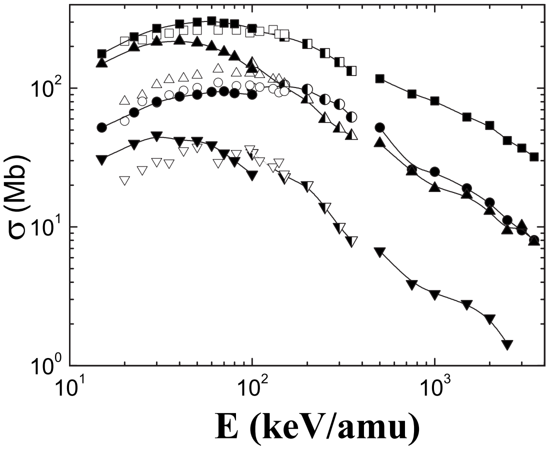

FIG. 3. H^+ impact cross sections leading to the formation of the target product channels H_2O^+, OH^+, O^+, and H^+. Pure ionization ${}_{10}\sigma_{11}$: present high-energy data—filled symbols; Gobet *et al.* [11,12]—open symbols. Combined pure ionization and transfer ionization, ${}_{10}\sigma_{11}+{}_{10}\sigma_{02}$: present low-energy data—filled symbols; Werner *et al.* [10]—left-filled symbols. Key: squares—H_2O^+; up triangles—H^+; circles—OH^+; inverted triangles—O^+. Error bars are not shown for the sake of clarity.

H^+ channel are almost as abundant as those for the H_2O^+ channel and both are closely followed by the OH^+ channel. The O^+ channel remains smaller but, around this energy, the difference is reduced to one order of magnitude.

The electronic configuration and term of the ground state of the H_2O molecule is given by $(1a_1)^2$ (core), $(2a_1)^2$ (inner-valence orbital), $(1b_2)^2(3a_1)^2(1b_1)^2$ (outer-valence orbitals), X^1A_1.

According to Tan *et al.* [22], Olivera *et al.* [23], Luna and Montenegro [24], and Montenegro *et al.* [25], the branching ratios for the water fragmentation pattern is related to the probabilities of removing electrons from the $1b_1$, $3a_1$, $1b_2$, and $2a_1$ molecular orbitals of water. The $1b_1$, $3a_1$, $1b_2$, and $2a_1$ levels have vertical ionization energies of 12.61, 15.57, 19.83, and 36.88 eV, respectively, and the removal of electrons from these levels progressively favors the production of the H_2O^+, OH^+, H^+, and O^+ channels. Table III reproduces the branching ratios given by Tan *et al.* [22] to help the reader when an electron from a specific orbital is removed. In the case of electron capture, the low-velocity cross sections are strongly dependent on the energy required to remove the orbital electrons (Knudsen *et al.* [26]), favoring the removal of the outermost electrons and making the H_2O^+ production the dominating channel. As the collision energy increases, electron capture becomes less sensitive to the binding energy and start to remove deep orbital electrons. At high energies, the one-electron cross sections for H_2O^+, OH^+, H^+, and O^+ production should thus start to exhibit a fixed ratio to each other, as indicated by Fig. 2.

TABLE III. Dissociation probabilities (in %) reported by Tan *et al.* [22] when a single $1b_1$, $3a_1$, $1b_2$, or $2a_1$ electron is removed by photons.

Ion	$1b_1$	$3a_1$	$1b_2$	$2a_1$
H_2O^+	100	100	8	
OH^+			70	
H^+			22	74
O^+				26

Similar measurements of Gobet *et al.* [11,12] are also included in Fig. 2, and as can be seen their data, the H_2O^+ and H^+ channels are in excellent agreement with our similar cross sections both in magnitude and in energy dependence. Their cross sections for the OH^+ and O^+ channels, however, agree with ours only in the energy dependence and are, respectively, about a factor of 1.2 and 1.4 higher than the present data. These authors state that, because of their use of a small acceptance geometry, their collection efficiency was 100% only for the parent H_2O^+ ions and, so, they multiplied their H^+, O^+, and OH^+ ion measurements by factors of 3.07, 1.68, and 1.29, respectively, to bring them individually into agreement with the cross sections of Werner *et al.* [10]. Our data shown in Figs. 2 and 3 contain no such species-dependent correction factors. For our high-energy measurements shown in Fig. 3, we used a flight distance of 300 mm in conjunction with a strong extraction field of 960 V/cm to provide fully resolved mass spectra with almost equal collection efficiency for all the H_2O^+, OH^+, H^+, and O^+ ions. For our low-energy measurements in Figs. 2 and 3, we used three different flight distances. We used a flight distance of 240 mm to provide TOF spectra with a reasonably good resolution between the O^+, OH^+, and H_2O^+ peaks; a flight distance of 70 mm for a reasonable resolution but sufficient to check if the O^+ or the OH^+ signals, obtained using fitting procedures, were being lost at the flight distance of 240 mm. We found no change in the OH^+ and a small change in the O^+ signals. The relatively large uncertainty in determining the O^+ peak at the flight distance of 70 mm is reflected in the large error bars quoted in Tables I and II for this channel. Finally, we used a flight distance of 30 mm to ensure that most of the H^+ ions, including those carrying high dissociation energy components, were collected efficiently. Our target ion detector area was 25 mm in diameter.

In Fig. 3 we show our cross sections for collisions involving ionization. Our high-energy measurements were carried out using target-ion–incident-proton coincidences and correspond to the pure ionization cross sections ${}_{10}\sigma_{11}$. Our low-energy measurements were carried out using target-ion–target-electron coincidences and the measured cross sections *e* correspond to the combination of the pure ionization cross sections ${}_{10}\sigma_{11}$ and the transfer-ionization cross sections ${}_{10}\sigma_{02}$ where the projectile captures one target electron and ionizes a second one.

The 100 to 350 keV measurements of Werner *et al.* [10] are included in Fig. 3. They used a target-ion–target-electron coincidence arrangement and, thus, their measurements strictly correspond to the combined ${}_{10}\sigma_{11}+{}_{10}\sigma_{02}$ cross sections. It can be seen that our low-energy data are in a remarkably good agreement with Werner *et al.* [10] for all the channels except the O^+ one, which is in agreement within the combined errors of the two sets of measurements. Our high-energy pure ionization cross sections ${}_{10}\sigma_{11}$ are also in close agreement with the high-energy data of Werner *et al.* [10]. At

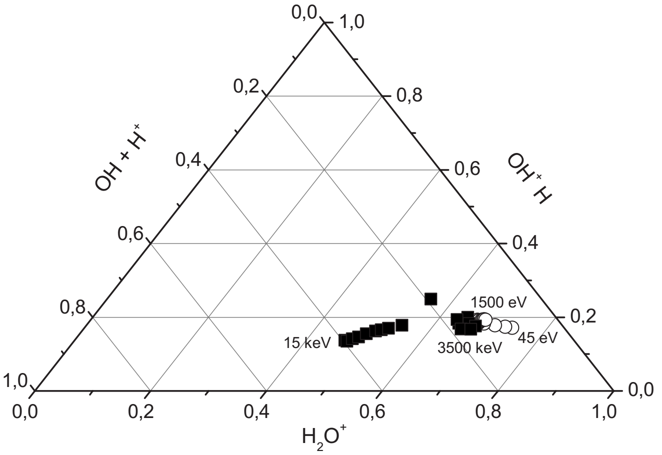

FIG. 4. Ternary graph for the single ionization of water by 15–3500 keV proton (squares) and 45–1500 eV electron (circles) impact. Proton data is from this work and electron data is from Scully *et al.* [28] (see also Montenegro *et al.* [25]).

energies well beyond 100 keV, the transfer-ionization cross sections $_{10}\sigma_{02}$ are expected to be negligible compared with the pure ionization cross sections, $_{10}\sigma_{11}$, and for this reason the excellent agreement observed is not too surprising.

It is clear from Fig. 3 that, for energies beyond 200 keV, there is a definite constancy in the ratios between the four ionization channels, with the cross sections obeying the relationship $H_2O^+ > OH^+ \approx H^+ > O^+$. This energy-independent behavior in the cross section ratios is an indication that a single collision event populating an excited H_2O^+ molecular ion is involved at high collision energies with the excited state subsequently decaying to a number of possible fragment channels with fixed branching ratios. Such a dissociation pattern has also been observed in the ionization of CH_4 molecules by proton and electron impact [27].

The branching ratios for the H_2O^+, OH^+, H^+ production are better visualized through the ternary graph shown in Fig. 4, where the major products of ionization of water obtained in the present proton work and our previous electron impact experiments (Scully *et al.* [28], Montenegro *et al.* [25]) are shown. It is clear that, at high velocities, the branching ratios for both projectiles coalesce approximately at 67% of H_2O^+, 18% of OH^+, and 15% of H^+. As described by Montenegro *et al.* [25], these ratios are associated with the high-energy behavior of the ionization cross section by a bare projectile, i.e., $\sigma_i \sim (1/I)\,(\ln E)/E$, where E is the projectile energy and I is the ionization potential, which gives a $1/I$ dependence for the vacancy production among the various molecular orbitals, independent of the projectile energy. Combining this dependence of the vacancy production and the ionization potential, with the fragmentation branching ratios of Tan *et al.* [22] given in Table III, we obtain 68.9% of H_2O^+, 16.5% of OH^+, and 14.6% of H^+, in close agreement with our measurements.

At low velocities, on the other hand, the fragmentation fractions for ionizing collisions are very different for incident electrons and protons. For both these projectiles, the cross sections for ionizing the outermost levels increase steeply relatively to the innermost ones with decreasing velocity, and the H_2O^+ production, which comes mostly from the $1b1$ and $3a1$ orbitals, increases accordingly. This reasoning explains the behavior shown in Fig. 4 for the case of electrons. For protons, electron capture is also a possible collision process which also removes the $1b_1$ and $3a_1$ electrons in this velocity range. It is in direct competition with ionization and dominates at low velocities with the consequence that at low velocities, the production of H_2O^+ as a final product of the single ionization channel is greatly inhibited. The different dynamical behavior of electrons and protons at low velocities are clearly apparent in Fig. 4. The pure ionization measurements of Gobet *et al.* [12] for $_{10}\sigma_{11}$ obtained using a target-ion–incident-proton coincidence arrangement are also included in Fig. 3 overlapping our low-energy measurements. A direct comparison of our low-energy cross sections with Gobet *et al.* [12] is not possible since our cross sections include contributions from the transfer-ionization cross sections $_{10}\sigma_{02}$. As noted above, Gobet *et al.* used large correction factors to renormalize their H^+, O^+, and OH^+ data and this procedure would introduce large errors in the absolute values of their cross sections for the channels leading to the formation of these fragments. Despite these large errors, it is clear from Fig. 3 that simple comparisons of the Gobet *et al.* [12] $_{10}\sigma_{11}$ cross sections with our combined $_{10}\sigma_{11}+{}_{10}\sigma_{02}$ cross sections can allow us to draw several useful conclusions on the importance of the transfer-ionization process $_{10}\sigma_{02}$ and the decay pathway that would result from such a collision. For instance, for the channel leading to H^+ formation, our combined $_{10}\sigma_{11}+{}_{10}\sigma_{02}$ cross sections are considerably larger than the $_{10}\sigma_{11}$ cross sections of Gobet *et al.* [12]. It is also clear that, for the channel leading to OH^+ formation, our combined $_{10}\sigma_{11}+{}_{10}\sigma_{02}$ cross sections and the $_{10}\sigma_{11}$ cross sections of Gobet *et al.* [12] are nearly equal over the whole of our common energy range. It is apparent that, for the channel leading to O^+ formation, our combined $_{10}\sigma_{11}+{}_{10}\sigma_{02}$ cross sections are larger than the Gobet *et al.* [12] $_{10}\sigma_{11}$ cross sections but not to the same extent as those for the H^+ channel. A conclusion which can be drawn from the above observations is that the transfer-ionization process $_{10}\sigma_{02}$ seems to preferentially populate the H^+ channel. It also seems to become a major ionization channel below the collision energy of about 50 keV and, at our lowest energies, seem to become comparable to the ionization channel leading to H_2O^+ formation. It should be noted that double ionization also enhances the H^+ production at high velocities, as can be inferred using equivelocity electron-impact cross sections measured by Scully *et al.* [28].

Since transfer-ionization involves the removal of two electrons (three-electron removal is also possible but unlikely over our low-energy range), these observations give important insights into the fragmentation pathways that the doubly ionized H_2O^{2+} molecule would undergo in contrast to the pathways followed by a singly ionized water molecule in an excited state, formed at very high collision energies, as discussed above [23]. For a doubly ionized water molecule, we suggest the following initial fragmentation stage:

$$H_2O^{2+} \rightarrow H^+ + (OH^+)^*. \qquad (6)$$

As can be seen in Fig. 3, our combined ${}_{10}\sigma_{11}+{}_{10}\sigma_{02}$ cross sections for the channel OH^+ are almost of the same value as the ${}_{10}\sigma_{11}$ cross sections of Gobet *et al.* [12]. This suggests that transfer-ionization contributions to the OH^+ channel from Eq. (6) are negligible and the OH^+ formed in Eq. (6) must be unstable and give rise to further fragmentation pathways such as

$$(OH^+)^* \rightarrow H^0 + O^+ \tag{7a}$$

or

$$(OH^+)^* \rightarrow H^+ + O^0, \tag{7b}$$

with specific branching ratios for either the (7a) or (7b) paths. Path (6) followed by path (7a) would, then, give rise to the production of H+ and O+ ions, while path (6) followed by path (7b) would produce two H+ ions. It is worth pointing out that when two ions are produced in a single collision, our TOF electronics was such that it only recorded the first ion detected. So, if our detector had a 100% detection efficiency, the H^+ ions from path (6) would be the only ones detected. However, in our recent electron impact measurements of double ionization of water by Scully *et al.* [28], it was found that the detection efficiency of a similar type of microchannel plate detector assembly as the one used here was around 17%. Assuming that our present detector also has a detection efficiency of about this value, then path (6) followed by path (7a) would provide a signal recording 17% of the time to the H^+ channel and 14% of the time to the O^+ channel, while path (6) followed by path (7b), on the other hand, would provide a recording 31% of the time exclusively to the H^+ channel. Since our combined measured ${}_{10}\sigma_{11}+{}_{10}\sigma_{02}$ cross sections for the H^+ channel are much larger than the ${}_{10}\sigma_{11}$ cross sections of Gobet *et al.* [12] for the same channel, this suggests that the latter path combination is the most probable dissociation pathway for doubly ionized water. Our finding also suggests that the unstable excited $(OH^+)^*$ ion relaxes preferentially by the ejection of an H^+ ion. Note that this scenario is associated to low-velocity impact, in which the two removed electrons come preferentially from the outermost molecular levels.

In Fig. 5 we compare our one-electron capture cross sections and our combined ${}_{10}\sigma_{11}+{}_{10}\sigma_{02}$ cross sections summed over all the target product channels with the similarly summed ${}_{10}\sigma_{11}$ cross sections of Gobet *et al.* [12] and the combined ${}_{10}\sigma_{11}+{}_{10}\sigma_{02}$ cross sections of Werner *et al.* [10], together with the total one-electron capture cross sections σ_c and the cross sections σ_+ for total positive target ion production measurements of Rudd *et al.* [9]. It can be seen that our summed capture cross sections are in excellent agreement with those of Rudd *et al.* [9] and Gobet *et al.* [12], while our high energy ${}_{10}\sigma_{11}$ cross sections are in excellent agreement with the σ_+ cross sections of Rudd *et al.* [9] and the combined ${}_{10}\sigma_{11}+{}_{10}\sigma_{02}$ cross sections of Werner *et al.* [10]. This good agreement with Rudd *et al.* [9] and Werner *et al.* [10] leads further support to the fact that our experimental setup had successfully collected all the target products with a high efficiency. Because of the ${}_{10}\sigma_{02}$ contributions, our low-energy combined ${}_{10}\sigma_{11}+{}_{10}\sigma_{02}$ cross sections are, not surprisingly, higher than the ${}_{10}\sigma_{11}$ cross sections of Gobet *et al.* [12]. Similarly, our combined data of the capture and the ionization channels are slightly higher than the low-energy σ_+ cross sections of Rudd *et al.* Transfer-ionization contributions are recorded in both our capture and ionization measurements and are, thus, included twice in our combined cross sections.

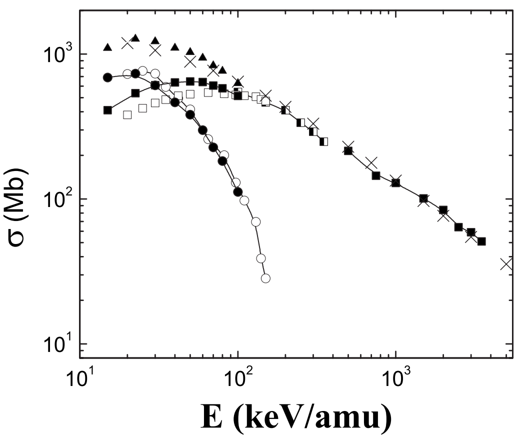

FIG. 5. H^+ impact total cross sections summed over all target product channels. One-electron capture cross sections ${}_{10}\sigma_{01}+{}_{10}\sigma_{02}$: present—full circles; Gobet *et al.* [11,12]—open circles. Pure ionization cross sections ${}_{10}\sigma_{11}$: present high-energy data—filled squares; Gobet *et al.* [11,12]—open squares. Combined transfer ionization and pure ionization ${}_{10}\sigma_{11}+{}_{10}\sigma_{02}$: present low-energy data—filled squares; Werner *et al.* [10]—half-filled squares. Also included are the total Rudd *et al.* [9] cross sections for capture σ_{10}—star symbol, and total target positive ion production σ^+—cross symbols, as well as present combined cross sections for the capture and the ionization channels summed over all target products—triangles. Error bars are not shown for the sake of clarity.

B. Neutral hydrogen impact

Our H^0 impact cross sections for the dissociative and the nondissociative channels resulting from target electron loss through ionization and one-electron capture collisions, as well as collisions where the projectile also loses its electron, are shown in Figs. 6–9 and are also tabulated in Tables IV–VI, respectively, over the energy range from 15 to 100 keV. The error bars included in the tables are due mainly to the fact that the H_2O^+, OH^+, and O^+ peaks were only partially resolved in our TOF spectra and are highest for the O^+ channel.

The H^0 impact cross sections for target electron loss through ionization are shown in Fig. 6. The channel leading to the H_2O^+ ion formation is dominant over the whole of the present energy range. This behavior can be explained by noting that only soft collisions, ionizing the external electrons, are able to keep the H^0 intact.

As discussed before, the selective removal of the outermost electrons enhances the production of H_2O^+ compared to the other fragments. The H^+ channel is about 60% of the H_2O^+ channel at 100 keV and presents a peak around 35 keV before falling to about 30% of the H_2O^+ channel at 15 keV. The OH^+ channel is 34% of the H_2O^+ one at 100 keV and, unlike the H^+ channel, continues to rise with

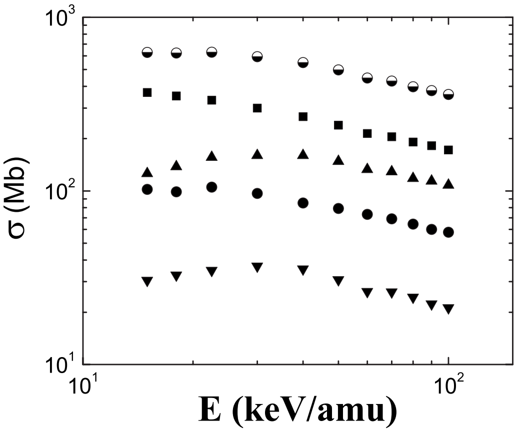

FIG. 6. H^0 impact ionization cross sections for the combination ${}_{10}\sigma_{11}+{}_{10}\sigma_{02}$ leading to the formation of the target products H_2O^+, OH^+, O^+, and H^+. Black squares—H_2O^+ channel; black circles—OH^+ channel; black up triangles—H^+ channel; black inverted triangles—O^+ channel; bottom filled circles—summed ionization cross sections over all target product channels. Error bars are not shown for the sake of clarity.

decreasing energy, reaching 28% of the H_2O^+ channel at 15 keV. The O^+ channel is one order of magnitude smaller than the H_2O^+ one and has a broad maximum at around 40 keV. In Fig. 7 we show our H^0 impact cross sections resulting from one-electron capture collisions. Comparison with Fig. 6 shows that these cross sections are about one order of magnitude smaller than the ionization ones. The cross sections for the H_2O^+ channel are the largest and rise much more rapidly with decreasing energy than the ionization cross sections for the same channel. The cross sections for the OH^+ and the H^+ channel are of similar magnitude, with the latter larger at 100 keV and the former at the energy of 8 keV. The O^+ channel is the weakest and has a broad peak at an energy around 40 keV. In Fig. 8 we show our H^0 impact cross sections for target ionization where the projectile also looses an electron (henceforth known as electron loss with target ionization). Large amounts of energy have to be transferred in these collisions to remove a target and a projectile electron and, consequently, these cross sections start to decrease rapidly at low collision energies. In these collisions, the H_2O^+ channel has the largest cross sections and is followed by the cross sections for the OH^+, H^+, and the O^+ channels, in this order.

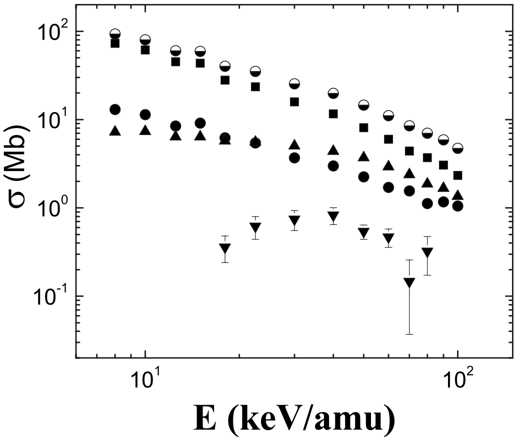

FIG. 7. H^0 impact one-electron capture cross sections ${}_{00}\sigma_{-11}$ leading to the formation of the target products H_2O^+, OH^+, O^+, and H^+. Symbols are same as in Fig. 6. Only few error bars are shown for the sake of clarity.

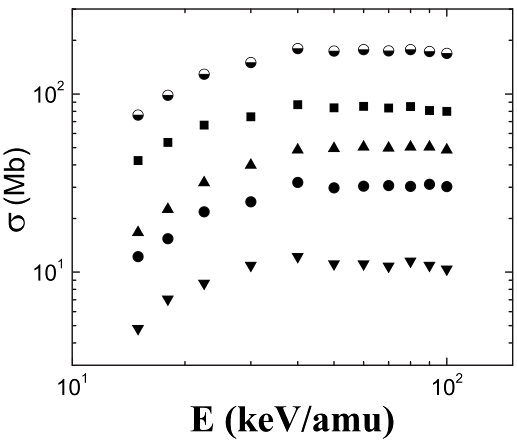

FIG. 8. H^0 impact cross sections ${}_{00}\sigma_{11}$ for projectile electron loss with target ionization leading to the products H_2O^+, OH^+, O^+, and H^+. Symbols are same as in Fig. 6. Error bars are not shown for the sake of clarity.

In Fig. 9 we compare our total cross sections for ionization, electron capture, and electron loss with target ionization for the H^0 projectiles summed over all the target ion channels. The ionization cross sections are the largest in the present energy range and, while those for electron capture are the lowest at high energies, they rapidly rise with decreasing energy and overtake cross sections for the electron

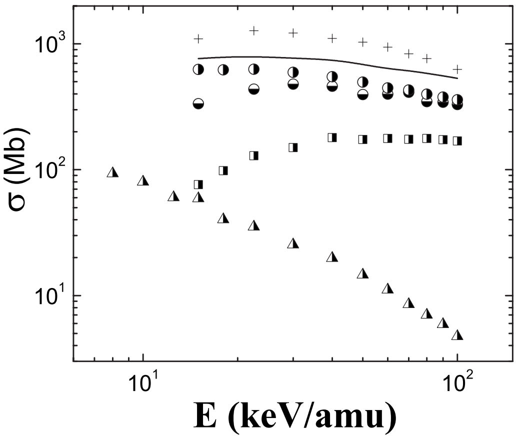

FIG. 9. Comparison of present H^0 impact total cross sections for ionization, one-electron capture and projectile electron-loss collisions obtained by summing individual cross sections for the H_2O^+, OH^+, O^+, and H^+ target channels. Right-filled circles—ionization, ${}_{00}\sigma_{01}$; right-filled triangles—one-electron capture, ${}_{00}\sigma_{-11}$; right-filled squares—projectile electron loss, ${}_{00}\sigma_{11}$. Present cross sections for projectile electron loss measured in noncoincidence mode $({}_{00}\sigma_{10}+{}_{00}\sigma_{11})$—bottom-filled circles, are included for comparison. Also included are the σ^+ cross sections for total positive target ion production by H^0 projectiles—solid line, and by H^+ projectiles—crosses. Error bars are not shown for the sake of clarity.

TABLE IV. Cross sections (in Mb) for the ionization of H_2O by 15 to 100 keV H^0 projectiles without measuring the projectile final state.

E (keV)	H_2O^+	OH^+	H^+	O^+
15	369±29	102±15	126±6	31±8
18	352±28	99±15	138±7	31±8
22.5	333±27	105±15	156±8	35±8
30	300±24	97±14	160±8	37±8
40	268±21	85±13	160±8	36±8
50	239±19	79±12	148±7	31±8
60	214±17	73±11	133±7	26±7
70	205±16	69±11	129±6	26±7
80	191±15	64±10	118±6	24±6
90	182±14	60±9	114±6	22±6
100	172±14	58±9	108±5	21±5

loss with target ionization. At very high energies the cross sections for electron loss with target ionization seem to show a trend of becoming comparable in magnitude to the ionization cross sections. We also show in Fig. 9 for comparison purposes, our total cross sections for the projectile electron loss channel only, measured using a noncoincidence mode. These cross sections include our coincidence-measured electron-loss cross sections with target ionization (right-filled squares in Fig. 9), and cross sections from collisions where the target produces no ionic species. A simple subtraction would show that the majority of the electron-loss collisions are accompanied by events in which the target is left with no charged components.

It is apparent from Figs. 5 and 9 that the ionization cross sections for H^0 projectiles continue to increase in magnitude with decreasing energy, in marked contrast to the cross sections obtained with proton projectiles, where the ionization cross sections reach a maximum at around 50 keV and fall rapidly on either side. At 15 keV, the total ionization cross section is nearly 4.1 Mb for incident protons and 6.3 Mb for incident H^0 projectiles, which might suggest that at low collision energies neutral hydrogen projectiles are more efficient in removing a target electron from water molecules than protons. However, other processes, such as electron capture, compete with ionization in the removal of a target electron and all these processes should strictly be considered for proper comparisons. In Fig. 9 we show, as a solid line, the sum of all our cross sections for the H^0 projectile which produce ionized target products and, as crosses, the similar cross sections for proton projectiles. As expected, the total electron removal cross sections by protons are larger than for H^0 projectiles but, surprisingly, the differences are within a factor of 1.5, meaning that protons are only marginally more efficient.

TABLE V. Cross sections (in Mb) for one electron capture by 8 to 100 keV H^0 projectiles in H_2O.

E (keV)	H_2O^+	OH^+	H^+	O^+
8	73±6	13±2	7.2±0.4	
10	61±5	11±2	7.3±0.4	
12.5	45±4	8.4±1.3	6.4±0.3	
15	44±4	9.1±1.4	6.4±0.3	
18	28±2	6.2±0.9	5.8±0.3	0.36±0.12
22.5	23.5±1.9	5.4±0.8	5.6±0.3	0.62±0.18
30	15.9±1.3	3.7±0.6	5.1±0.2	0.74±0.19
40	11.6±0.9	3.0±0.5	4.4±0.2	0.83±0.18
50	8.1±0.6	2.3±0.3	3.7±0.2	0.54±0.10
60	6.0±0.5	1.7±0.3	2.9±0.2	0.47±0.11
70	4.4±0.4	1.6±0.2	2.4±0.1	0.15±0.11
80	3.7±0.3	1.1±0.2	1.9±0.1	0.32±0.15
90	3.1±0.2	1.2±0.2	1.7±0.1	
100	2.3±0.2	1.1±0.2	1.4±0.1	

TABLE VI. Cross sections (in Mb) for the ionization of H_2O by 15 to 100 keV H^0 projectiles together with projectile electron loss.

E (keV)	H_2O^+	OH^+	H^+	O^+
15	42±12	12±4	17±5	4.7±1.8
18	53±12	15±4	23±5	7.0±1.9
22.5	67±9	22±5	32±4	8.7±2.5
30	74±8	25±5	40±4	11±3
40	87±8	32±6	49±3	12±3
50	84±8	30±6	50±3	11±3
60	85±8	30±6	50±3	11±3
70	83±8	31±6	50±3	11±3
80	85±8	30±6	50±3	12±3
90	81±8	31±6	50±3	11±3
100	80±8	30±6	49±3	10±3

In a recent work, Gobet *et al.* [29] carried out total cross section measurements of projectile electron loss using a noncoincidence mode (projectile channel only) and using coincidences with target ions without mass analysis. These cross sections are compared with our present measurements in Fig. 10 (which are tabulated in Table VII). Also included in Fig. 10 are the total electron-loss cross sections for projectile channel only of Dagnac *et al.* [30] and of Toburen *et al.* [8]. It can be seen that our electron-loss cross sections for the projectile channel only (left-filled circles) agree remarkably well with Dagnac *et al.* [30] and Toburen *et al.* [8]. The similar Gobet *et al.* [29] measurements are smaller than all these three sets of data at lower energies and higher at the high energies. For the coincidence measurements involving target ionization, the data of Gobet *et al.* [29] (black open squares) agrees well with our cross sections (black right-filled squares) at high energies, but falls much faster than ours at low energies. The electron loss with target ionization process requires energy to remove not only one of the target electrons but also the projectile electron. At low collision energies, the collision would need to be sufficiently violent to supply this energy with the consequence that the projectile would suffer large angular deflections. In the present work we used a 25 mm-diameter detector placed at a distance of 250 mm away from the interaction region to detect the fast

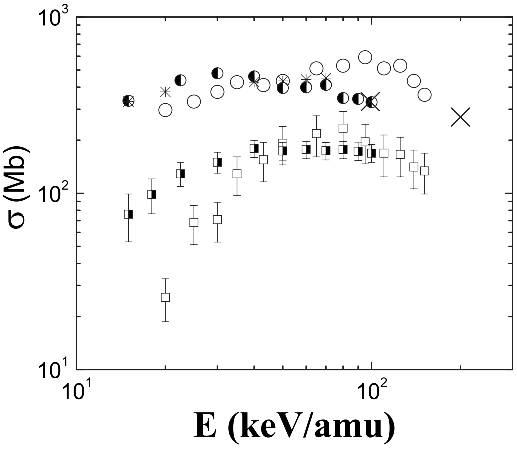

FIG. 10. Comparison of present H^0 impact cross sections for total projectile electron loss with previous measurements. Sum ${}_{00}\sigma_{10}+{}_{00}\sigma_{11}$ obtained through measurements without coincidences with target ion products: bottom-filled circles, present (same as in Fig. 9); open circles, Gobet *et al.* [29]; black stars, Dagnac *et al.* [30]; black crosses, Toburen *et al.* [8]. ${}_{00}\sigma_{11}$ using coincidence methods: right-filled squares present (same as in Fig. 8); open black squares, Gobet *et al.* [29].

protons products of the electron-loss collisions. Our full detector acceptance angle was, thus, over 5° and would be wide enough to collect all of the scattered protons. We used 100 mm-long electrostatic plates to separate the various projectile charge states. Gobet *et al.* [29] used magnetic deflection to separate their projectile charge states. This would imply that their projectile detector should be much further away than ours. It is, thus, probable that their detector could have missed many of the large-angle scattered protons prevalent at low collision energies.

IV. CONCLUSIONS

We have measured detailed cross sections of the dissociation pathways that water undergoes in electron capture and ionization collisions by fast protons and electron capture, ionization, and projectile electron loss by fast H^0 projectiles using a compact experimental apparatus incorporating a sufficiently high-resolution TOF spectrometer with the ability to collect majority of the diverging collision products.

Our data for H^+ projectiles at high energy shows a constant behavior of the branching ratios between the various pathways. We have shown that this result together with those of Werner *et al.* [10] and supported by the theoretical predictions of Olivera *et al.* [23], suggests that at high energies a single step collision process occurs which populates a highly excited H_2O^+ ion similar to those formed when an inner-shell electron is removed in photoionization. At low collision energies, on the other hand, we find that transfer-ionization is a strong process for proton projectiles, leading to the formation of an H_2O^{2+} ion. Our measurements indicate that this doubly ionized water molecule decays mainly through the emission of an H^+ ion, with the companion OH^+ ion remaining sufficiently excited, so that it too subsequently decays, ejecting either an H^+ ion or an O^+ ion, the first being the dominant channel.

TABLE VII. Total cross sections (in Mb) for the electron loss of the 15 to 100 keV H^0 projectiles in collision with H_2O without measuring the target final state.

E (keV)	Total electron loss
15	335±55
22.5	437±73
30	479±79
40	460±78
50	396±67
60	399±68
70	412±70
80	347±59
90	343±58
100	329±56

Our data for H^0 projectiles show that these neutral projectiles have much larger ionization cross sections compared with those for proton impact. When total removal of the target electron is considered, the neutral projectile is equally efficient as H^+ ions in removing a target electron, giving rise to a substantial amount of fragmentation. It is thus imperative, in any modeling of dose profiles in proton-based radiotherapy, that the damage caused by fast neutrals, formed from protons undergoing electron capture collisions, also has to be considered.

ACKNOWLEDGMENTS

The support of the UK Engineering and Physical Science Research Council (EPSRC) is gratefully acknowledged. E.C.M. and V.S. would like to thank the International Research Centre for Experimental Physics (IRCEP) at Queen's University Belfast. E.C.M., A.L.F.B., P.H.Y.G., A.M.S., and A.C.F.S. would also like to acknowledge support from the Brazilian Agencies CNPq and FAPERJ. One of us (H.L.) acknowledges support from the EU FP6 Marie Curie program and HEA North-South programme. J.A.W. acknowledges the Department of Education, Northern Ireland for additional support.

[1] D. T. Hall *et al.*, Science **373**, 677 (1995).
[2] B. C. Garrett *et al.*, Chem. Rev. (Washington, D.C.) **105**, 355 (2005).
[3] A. Brahme, Int. J. Radiat. Oncol., Biol., Phys. **58**, 603 (2004).
[4] E. J. Hall, *Radiobiology for the Radiologist*, 5th ed. (Lippincott, Williams, & Wilkins, Philadelphia, PA, 2000).
[5] H. Chang, W. Oehrl, P. Elsner, and J. J. Thiele, Free Radical Res. **37**, 655 (2003).

[6] H. Nikjoo, S. Uehara, I. G. Khvostunov, F. A. Cucinotta, W. E. Wilson, and D. T. Goodhead, Phys. Medica **17**, 38 (2001).
[7] S. Uehara, L. H. Toburen, W. E. Wilson, D. T. Goodhead, and H. Nikjoo, Radiat. Phys. Chem. **59**, 1 (2000).
[8] L. H. Toburen, M. Y. Nakai, and R. A. Langley, Phys. Rev. **171**, 114 (1968).
[9] M. E. Rudd, T. V. Goffe, R. D. DuBois, and L. H. Toburen, Phys. Rev. A **31**, 492 (1985).
[10] U. Werner, K. Beckord, J. Becker, and H. O. Lutz, Phys. Rev. Lett. **74**, 1962 (1995).
[11] F. Gobet, B. Farizon, M. Farizon, M. J. Gaillard, M. Carreé, M. Lezius, P. Scheier, and T. D. Mark, Phys. Rev. Lett. **86**, 3751 (2001).
[12] F. Gobet, S. Eden, B. Coupier, J. Tabet, B. Farizon, M. Farizon, M. J. Gaillard, M. Carreé, S. Ouaskit, T. D. Mark, and P. Scheier, Phys. Rev. A **70**, 062716 (2004).
[13] A. C. F. Santos, W. S. Melo, M. M. Sant'Anna, G. M. Sigaud, and E. C. Montenegro, Phys. Rev. A **63**, 062717 (2001).
[14] A. C. F. Santos, W. S. Melo, M. M. Sant'Anna, G. M. Sigaud, and E. C. Montenegro, Rev. Sci. Instrum. **73**, 2396 (2002).
[15] E. G. Cavalcanti, G. M. Sigaud, E. C. Montenegro, M. M. Sant'Anna, and H. Schmidt-Böcking, J. Phys. B **35**, 3937 (2002).
[16] H. Luna, M. Michel, M. B. Shah, R. E. Johnson, C. J. Latimer, and J. W. McConkey, J. Geophys. Res. **108**(E4), 5033 (2003).
[17] H. Luna, C. McGrath, M. B. Shah, R. E. Johnson, M. Liu, C. J. Latimer, and E. C. Montenegro, Astrophys. J. **628**, 1086 (2005).
[18] D. P. Almeida, N. V. C. Faria, F. L. Freire, Jr., E. C. Montenegro, and A. G. Pinho, Nucl. Instrum. Methods Phys. Res. B **24**, 228 (1987).
[19] H. B. Gilbody, R. Browning, R. M. Reynolds, and G. I. Riddell, J. Phys. B **4**, 94 (1971).
[20] A. B. Whittkower and B. H. Gilbody, Proc. Phys. Soc. London **90**, 353 (1967).
[21] F. Alvarado, R. Hoekstra, and T. Schlatholter, J. Phys. B **38**, 4085 (2005).
[22] K. H. Tan, C. E. Brion, Ph. E. Van deer Leeuw, and M. J. Van deer Leeuw, Chem. Phys. **29**, 299 (1978).
[23] G. H. Olivera, C. Caraby, P. Jardin, A. Cassimi, L. Adoui, and B. Gervais, Phys. Med. Biol. **43**, 2347 (1998).
[24] H. Luna and E. C. Montenegro, Phys. Rev. Lett. **94**, 043201 (2005).
[25] E. C. Montenegro, S. W. J. Scully, J. A. Wyer, V. Senthil, and M. B. Shah, J. Electron Spectrosc. Relat. Phenom. **155**, 81 (2007).
[26] H. Knudsen, H. K. Haugen, and P. Hvelplund, Phys. Rev. A **23**, 597 (1981).
[27] H. Luna, E. G. Cavalcanti, J. Nickles, G. M. Sigaud, and E. C. Montenegro, J. Phys. B **36**, 4717 (2003).
[28] S. W. J. Scully, J. A. Wyer, V. Senthil, M. B. Shah, and E. C. Montenegro, Phys. Rev. A **73**, 040701(R) (2006).
[29] F. Gobet, S. Eden, B. Coupier, J. Tabet, B. Farizon, M. Farizon, M. J. Gaillard, S. Ouaskit, M. Carreé, and T. D. Mark, Chem. Phys. Lett. **421**, 68 (2006).
[30] R. Dagnac, D. Blanc, and D. Molina, J. Phys. B **3**, 1239 (1970).